

PAPER • OPEN ACCESS

Simultaneous multi-material embedded printing for 3D heterogeneous structures


To cite this article: Ziqi Gao *et al* 2023 *Int. J. Extrem. Manuf.* **5** 035001

View the [article online](#) for updates and enhancements.

You may also like

- [A versatile embedding medium for freeform bioprinting with multi-crosslinking methods](#)
Qi Li, Zhuoran Jiang, Liang Ma et al.
- [Modeling the impact of granular embedding media and pulling versus pushing cells on growing cell clones](#)
Dirk Drasdo and Stefan Hoehme
- [A simple tissue clearing method for increasing the depth penetration of STED microscopy of fixed brain slices](#)
Julie Angibaud, Patrice Mascalchi, Christel Poujol et al.

Simultaneous multi-material embedded printing for 3D heterogeneous structures

Ziqi Gao^{1,2,4}, Jun Yin^{1,2,4}, Peng Liu^{1,2}, Qi Li^{1,2}, Runan Zhang³, Huayong Yang^{1,2} and Hongzhao Zhou^{1,2,*} 

¹ State Key Laboratory of Fluid Power and Mechatronic Systems, Zhejiang University, Hangzhou 310058, People's Republic of China

² School of Mechanical Engineering, Zhejiang University, Hangzhou 310058, People's Republic of China

³ Department of Mechanical Engineering, Centre for Power Transmission and Motion Control, University of Bath, Bath BA2 7AY, United Kingdom

E-mail: hz_zhou@zju.edu.cn

Received 29 December 2022, revised 8 February 2023

Accepted for publication 3 May 2023

Published 16 May 2023



Abstract

In order to mimic the natural heterogeneity of native tissue and provide a better microenvironment for cell culturing, multi-material bioprinting has become a common solution to construct tissue models *in vitro*. With the embedded printing method, complex 3D structure can be printed using soft biomaterials with reasonable shape fidelity. However, the current sequential multi-material embedded printing method faces a major challenge, which is the inevitable trade-off between the printed structural integrity and printing precision. Here, we propose a simultaneous multi-material embedded printing method. With this method, we can easily print firmly attached and high-precision multilayer structures. With multiple individually controlled nozzles, different biomaterials can be precisely deposited into a single crevasse, minimizing uncontrolled squeezing and guarantees no contamination of embedding medium within the structure. We analyse the dynamics of the extruded bioink in the embedding medium both analytically and experimentally, and quantitatively evaluate the effects of printing parameters including printing speed and rheology of embedding medium, on the 3D morphology of the printed filament. We demonstrate the printing of double-layer thin-walled structures, each layer less than 200 μm , as well as intestine and liver models with 5% gelatin methacryloyl that are crosslinked and extracted from the embedding medium without significant impairment or delamination. The peeling test further proves that the proposed method offers better structural integrity than conventional sequential printing methods. The proposed simultaneous multi-material embedded printing method can serve as a powerful tool to support the complex heterogeneous structure fabrication and open unique prospects for personalized medicine.

⁴ These authors contributed equally as first authors.

* Author to whom any correspondence should be addressed.



Original content from this work may be used under the terms of the [Creative Commons Attribution 4.0 licence](https://creativecommons.org/licenses/by/4.0/). Any further distribution of this work must maintain attribution to the author(s) and the title of the work, journal citation and DOI.

Supplementary material for this article is available [online](#)

Keywords: embedded printing, multi-material printing, printability, soft materials, heterogeneous structures

1. Introduction

Recently, the application of three-dimensional (3D) printing has been extended to tissue engineering by creating custom tissue constructs that contain tissue-specific cells for a closer mimic of the structure of native tissues [1–3]. Compared to other manufacturing technologies, 3D bioprinting has enabled better-controlled spatial distribution of cells and biomolecules in engineered structures, via the deposition of cell-laden bio-materials (bioinks) on the demand of computer-aided design models [4–6]. Conventional bioprinting technologies face several challenges, which may be concluded as the contradiction between overall mechanical stability and the biological microenvironment of the printed structures. Native organs and tissues in the human body are heterogeneous, containing various cell types and extracellular matrices components that provide diverse mechanical properties and biological environments for different cells. This heterogeneity plays a crucial role in the realization of the complex functions of organs and tissues. Researchers have come to realize that it is unrealistic to build fully functional tissues and organs *in vitro* with just a single material [7, 8]. As a solution to the current challenges, multi-material bioprinting technology provides different choices of cells and biomaterials for the *in vitro* construction of heterogeneous structures that may be a better representation of natural tissues and organs. At present, multi-material bioprinting technology has been used in the various biomanufacturing process including, skin, tendon, cartilage [9–12]. Multi-material printing, such as electronic printing, metal printing, ceramic printing, can also be used for manufacturing industrial parts and products [13–15]. In conventional bioprinting, rigid bioinks are required to support themselves to maintain a good shape fidelity, which can later impair cell viability, migration, and function [16, 17]. In order to resolve the contradiction between printability and biocompatibility, a new 3D printing technology, called embedded printing, has been developed. This method involves depositing bioinks within an embedding medium, which provides structural support through the yield stress and self-healing ability of the medium [18, 19]. As a result, low-stiffness bioinks can be printed and deposited continuously within the embedding medium. Multi-material embedded printing technology has been used for the manufacturing of hollow structures with overhanging and internal voids [20], the manufacture of tissue models [21], 4D printing and other research [22].

In the conventional direct ink writing in air, bioink is deposited on a platform to construct 3D structures in a stack-by-stack manner. With the effect of gravity, the extruded bioink

only stops when it reaches a solid surface, which guarantees adhesion between upper and lower layers (figure 1(a)). Due to its rheological properties, the deposited bioink cannot hold the defined shapes and may collapse, making it easy for neighbouring fibres to adhere in the horizontal direction. Therefore, the distance between the tip of the nozzle and the deposition plane, known as the stand-off distance, is normally greater than the height of a single layer of filaments. In the extrusion printing process, the velocity flow fields and shear rate fields are generated in the vicinity of the nozzle, which can be ignored for conventional printing in air. However, in embedded printing, shear stress is applied on the embedding medium, and makes it transfer from solid-like state to liquid-like state, known as Bingham plastic fluid. Because the embedding medium has much greater inertia than air, disturbances generated by the nozzle's movement can significantly impact the continuous deposition of the extruded bioink (figures 1(b) and (c)). Furthermore, the bioink is deposited into the embedding medium and remains almost stationary, limited to a small range before being contained within the embedding medium. This results in the bioink not collapsing within the bath. There is no guaranteed adhesion between adjacent filaments (figure 1(e)). It has been observed, in certain printing conditions, the filaments printed in sequence cannot be laterally attached as expected [23, 24]. A simple and commonly used solution is that the adjacent filaments are designed spatially overlapped to ensure that they can be connected with each other [25, 26]. The distances between the designed adjacent printing paths are less than the width of the printing filaments to achieve better lateral attachment of neighbouring filaments. The overlapping method has been proven effective when printing continuous structures with a single material. For complex structures with multiple materials, the overlapping of filaments may induce the uncontrolled stacking and squeezing of the adjacent filaments and jeopardize the spatial distribution of different materials in the printed structure. Therefore, the overlapping between different materials should be avoided in the printing of complex structures with good precision. It has been a challenge to print heterogeneous structures with precise material distribution while maintaining a reasonable overall structural integrity.

In this paper, we proposed a simultaneous multi-material embedded printing method that used individually controlled nozzles to construct multi-layered structures (figure 1(d)). Firstly, the dynamics of the extruded bioink in the embedding medium was analysed both analytically and experimentally, which enabled us to precisely control the deposition of the bioinks. Secondly, with multiple individually controlled

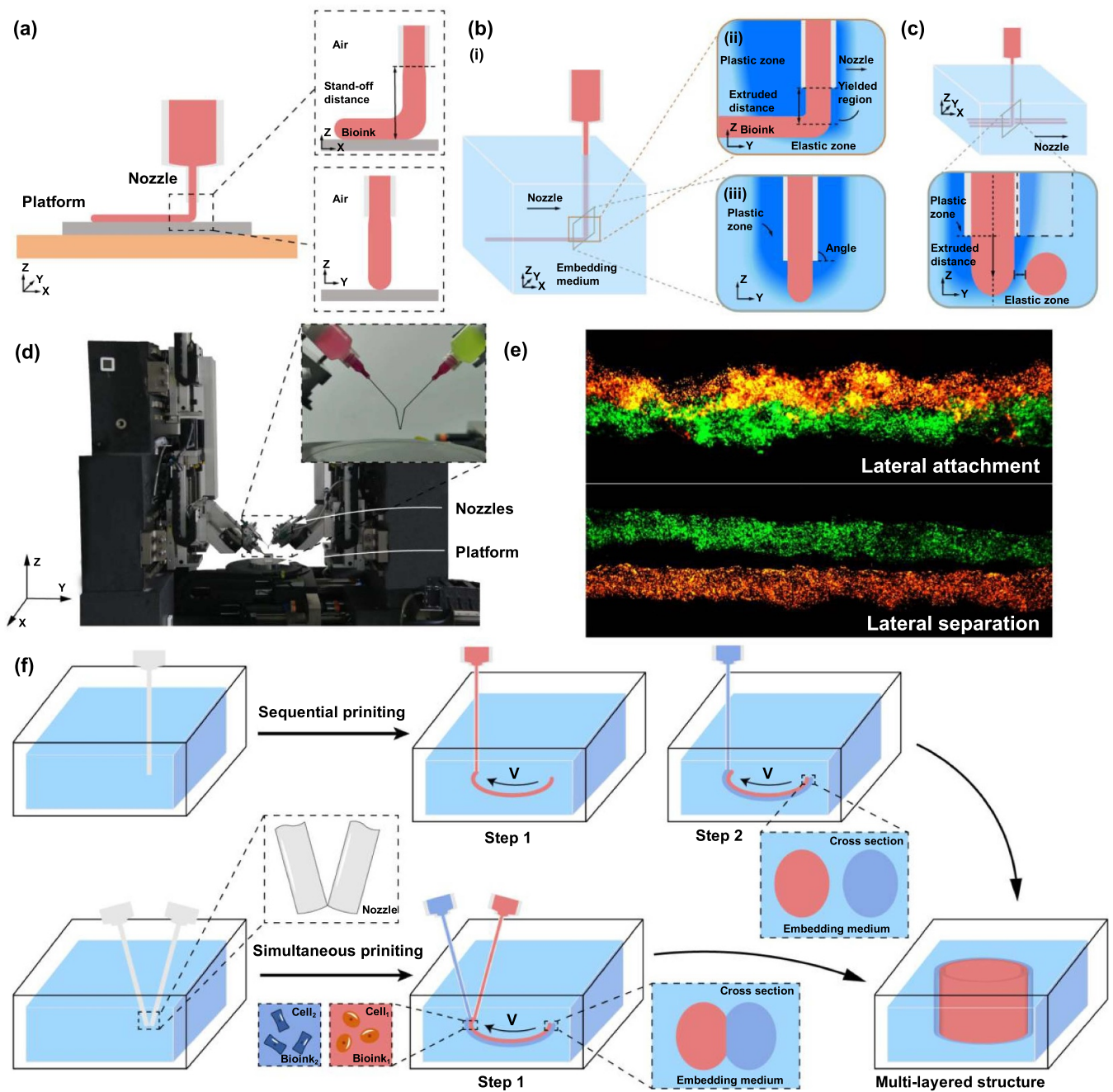


Figure 1. A schematic of simultaneous printing process (a) a schematic diagram of extruding process in the air. (b) A schematic diagram of extruding process in the embedding medium. (c) An illustration of horizontal separation of sequentially embedding printed filaments. (d) Multi-nozzle bioprinter. (e) Microfluorescence of the filaments with lateral attachment and lateral separation. (f) A comparison between sequential printing and simultaneous printing processes.

nozzles, different bioinks could be extruded simultaneously (figure 1(f)). Without overlapping the nozzles, the optimized system operation could allow the bioink to transport a certain distance and firmly fuse with each other. The squeezing and stacking behaviour of the bioinks were regulated, ensuring the effective adhesion between different materials and layers and attaining high printing fidelity. The effects of printing parameters, including printing speed and rheology of embedding medium, on the 3D morphology of the printed

filament were quantitatively evaluated. The proposed method was validated by printing double-layered hemisphere and tube structures with each layer less than 200 μm . Heterogeneous structures with complex morphology were further printed, including down scaled intestine and liver models with 5% gelatin methacryloyl (GelMA), all of which could be cross-linked and extracted from the embedding medium without significant impairment or delamination. Finally, a peeling test was carried out, which proved that the 3D structures

printed by the proposed simultaneous printing method had better structural integrity compared with those printed by the conventional sequential printing method.

2. Materials and methods

2.1. Preparation of the embedding medium, the bioink, and the removal bath

The embedding medium was comprised of the Pluronic F-127 (PF-127, Sigma-Aldrich, USA), and the hydrophobically modified hydroxypropylmethyl cellulose (H-HPMC, commercial name Sangelose 90L™, Daido Chemical Co., Japan). The PF-127 powder was dissolved in 1× phosphate buffer saline (1× PBS) and stored overnight at 4 °C. The PF-127 solution was heated to 50 °C with agitating in a magnetic stirrer, then the H-HPMC powders were gradually added to the PF-127 solution which was stirred at a speed of 800 rpm. Once the powder was completely dissolved, the temperature of the magnetic stirrer was then decreased to room temperature (RT, 26 °C) gradually with continuous low-speed stirring. Foam was removed from the surface of the embedding medium. The embedding medium was then transferred into a transparent box.

GelMa (EFL-GM-60, China) was used to prepare the bioink. In this study, 5% (w/v) GelMA was prepared by dissolving GelMA in 1× PBS containing 0.5% (w/v) lithium phenyl-2,4,6-trimethylbenzoylphosphinate (LAP, EFL, China) at 37 °C for 2 h. 0.1% (w/v) fluorescent particles (4 μm in diameter, Beisile, China) with different excitation wavelength were added into the GelMA solution respectively to observe the morphology of the printed filament. For better observation of the printed structures, 0.1% (w/v) food dyes with different colour were added into the GelMA solution respectively.

The polyethylene glycol 400 (PEG400, SCR, China) was used as removal baths. Five percentage (v/v) PEG400 was dissolved in 1× PBS with continuous oscillation until forming homogeneous solution.

2.2. Rheological measurements

A rotational rheometer (MCR102, Anton Paar, Austria) equipped with a parallel plate rotator (25 mm diameter) was used for rheological measurements. The gap was set at 1 mm for all tests. In rheological measurements, various concentrations of H-HPMC/PF-127 (2.5%/10%, 3%/9%, 3%/10%, 3%/11%, 3.5%/10%) were used. The ambient temperature of our printing experiments was controlled at 26 °C. Therefore, the steady shear rheology measurements were performed at 26 °C by increasing the shear rate from 0.01 to 100 s⁻¹. The embedding medium material could be modelled as a Herschel–Bulkley fluid, which is expressed as follows:

$$\tau = \left(K|\dot{\gamma}|^{n-1} + \frac{\tau_y}{\dot{\gamma}} \right) \dot{\gamma} \text{ for } \tau > \tau_y \quad (1)$$

$$\dot{\gamma} = 0 \text{ for } \tau \leq \tau_y \quad (2)$$

where τ is the shear stress, τ_y is the yield stress, $\dot{\gamma}$ is the shear rate, K is the consistency index, and n is the flow index [27]. The dependence of shear stress and viscosity on shear rate could be obtained. The thixotropy of the embedding medium was assessed by measuring the viscosity in transient shear rate step tests at 26 °C. Samples were subjected to a 0.1 s⁻¹ shear rate for 60 s, a 10 s⁻¹ shear rate for 10 s and a 0.1 s⁻¹ shear rate for 60 s to simulate the printing process (figure S1).

2.3. Simultaneous printing in the embedding medium

A bespoke bioprinter with up to six individually controlled nozzles was used [8]. Prior to printing, bioinks (5% GelMA with different fluorescent particles) were transferred into multiple 10 ml syringes and the syringes were installed on the nozzles (figure S2). The temperature of bioink was controlled at 26 °C under all experimental conditions. Two sets of embedding mediums were used, including 3% H-HPMC and variable PF-127 contents (9%, 10%, 11%) and variable H-HPMC contents (2.5%, 3.5%). In addition, 80 kPa extrusion pressure with a 25-gauge (25G) nozzle was utilized. The angle of the nozzle respect to the horizontal plane was adjustable from 60° to 80°. Under different printing conditions, printing velocity steps (2, 4, 8, 12, 16, and 20 mm s⁻¹) and embedding medium with different proportions to explore whether the filaments would attach. For linear 2D samples, the two nozzles moved at the same speed along the Y axis and the bioinks were extruded out by applying pressure while the X and Z axis positions were unchanged. The printed filaments were designed to be 20 mm in length before exposed to a UV light source (405 nm, 25 mW m⁻²) for 1 min. The filaments were removed from the embedding medium using the 5% (v/v) PEG400 removal bath at RT. We selected the middle of the printing filament for analysis in order to exclude the impact of the extrusion start and stop process on the experimental results. The printed filaments were placed on a slide and observed with a fluorescence microscope (DM IL LED, Leica, Germany). When no black area was found between the fluorescence areas in 80% or more length along the axial direction in the filament, the simultaneously printed filaments were considered to be attached.

In order to better investigate the morphology of printed filaments, imaging of the filaments was taken using a confocal laser scanning microscopy (Leica TCS SP8, German) or inverted fluorescence microscopy (DM IL LED, Leica, Germany). The fluorescent particle of the image in each z -stack during the 3D scan were extracted by MATLAB. Combining the x and y information of the image and the z information of the image, the fluorescent particle contour was reconstructed in 3D space (figure S3). The outermost contour formed by the fluorescent particle was considered as the two-dimensional morphology of the filament. The width of the filament was measured as the largest length of the filament in horizontal direction. Aspect ratio was evaluated according to the shape of the contour. The average value of the obtained data was taken as the estimation value of the width and aspect ratio of the whole filament.

2.4. Multi-layer 3D structure printing

To print three-dimensional structures using simultaneous printing methods, the 3D models were designed using SolidWorks, followed by slicing by Cura 4.7 with 0.2 mm layer height and manually reprogrammed for the simultaneous printing. The printing process was shown as the figure S4. The bioinks (5%GelMA with different food dye) was used. To print complex structures, the bioink was deposited into the embedding medium (10% PF-127 and 2.5% H-HPMC) in a transparent box, using 80 kPa pressure, 8 mm s⁻¹ velocity, and 25 G nozzles. To eliminate the boundary effect in the process of bioprinting, the three-dimensional structure was printed in the centre of the box. When completed, the embedded structure was exposed to a UV light system (405 nm, 25 mW m⁻²) for 5 min. The steps for extracting the structure were the same as mentioned. Then, the structure was transferred into 1× PBS. The structure was dissected along the axial direction and observed with an optical microscope to evaluate the characteristics of the simultaneous printing method with multi-materials. Bioinks with different crosslinking methods and rheological properties (5%w/v GelMA and 3%w/v Alginate) were also used for printing multi-layer 3D structures in 10% PF-127/3% H-HPMC embedding medium with 0.1% CaCl₂ added.

2.5. Peeling sample testing

In order to quantitatively investigate the adhesion of the two bioinks in the simultaneous printing process, a peeling test was conducted. In order to compare with the simultaneous printing method, we prepared the specimen printed by sequentially under the same trajectory and the samples by casting. Specimen test methods were based on ASTM D1876-08: standard test method for peel resistance of adhesives (T-peel test). Two strips were pulled apart from an initially T-shaped sample using a universal testing machine (ElectroForce 3200, TA Instruments, USA) [28]. One side of the sample was firstly secured in the upper grip. The free side of the sample was allowed to rest naturally, before it was secured in the lower grip. The upper grip was then fine-tuned upward until the secured part straighten, but with no initial tension (figure S6). The peeling test was performed with a constant ramp of 1 mm min⁻¹ until the sample failure happened or the maximum test range reached. The recorded data were tensile force, time, and displacement. Force data was normalized to the average width of each sample interface. And the peel properties were presented by variation of adhesion force, form of adhesion failure and average interfacial toughness.

2.6. Statistical analysis

Data was presented as mean ± standard deviation of independent replicates. Statistical analysis was conducted using one-way ANOVA. All analyses were performed using the 'R' statistical package using R-Studio v 1.4.1103. The *p* values were provided and significance levels are as follows:

*(*p* < 0.05), **(*p* < 0.01), ***(*p* < 0.001), ****(*p* < 0.0001). NS indicates no significant differences between groups (*p* > 0.05).

3. Results and discussions

3.1. The extrusion printing and precise deposition in embedding medium

The dynamics of the extruded bioink in the embedding medium is essential to structural integrity and printing precision in making complex 3D structures but have been rarely discussed in the literature. This section aims to investigate the bioink deposition process, from the moment bioink exits the nozzle until a steady state is reached, in which the relative speed between the printed filament and its surrounding embedding medium is zero (figure 2(a)). A simplified model is built, with the following assumptions: (a) both the bioink and the embedding medium are incompressible, (b) the deposition process is adiabatic, (c) the viscosity of embedding medium varies as a gradient induced by the shear rate gradient around moving nozzles, (d) the viscosity of the bioink remains constant after extrusion, and there is no velocity gradient within the analysed bioink.

For a constant printing speed in a specific embedding medium, the shear rate field and viscosity field around the nozzle could be approximated. Thus, by knowing the extrusion pressure, the bioink travel distance in the embedding medium could be analysed for a selected micro-mass unit. According to the Newton's second law and the law of conservation of mass, the following equation was satisfied when the bioink was extruded into the suspension medium to form a stable filament:

$$F + (mg - \rho_{\text{bath}}gV)\sin\alpha - \mu A \frac{v}{l} = m \frac{dv}{dt} \quad (3)$$

where *F* is the force transferred by bioink during extrusion, *m* is the mass of the extruded bioink, ρ_{bath} is the density of the embedding medium, *V* is the volume of the extruded bioink, α is the angle of the nozzle with respect to the horizontal plane, μ is the viscosity of the embedding medium, *A* is the surface area of the extruded bioink, *v* is the velocity of the extruded bioink, *l* is the size of the region where the embedding medium is yielded. Integrating equation (3) from time *t* to *t*₁ gives:

$$\int_{v_1}^v F + (mg - \rho_{\text{bath}}gV)\sin\alpha - \mu A \frac{v}{l} = \int_{v_1}^v m \frac{dv}{dt}. \quad (4)$$

The velocity of the extruded bioink could be determined as:

$$v = \frac{Fl + (mg - \rho_{\text{bath}}gV)l\sin\alpha}{\mu A} \left(1 - e^{-\frac{\mu A(t-t_1)}{ml}} \right) + v_1 e^{-\frac{\mu A(t-t_1)}{ml}}. \quad (5)$$

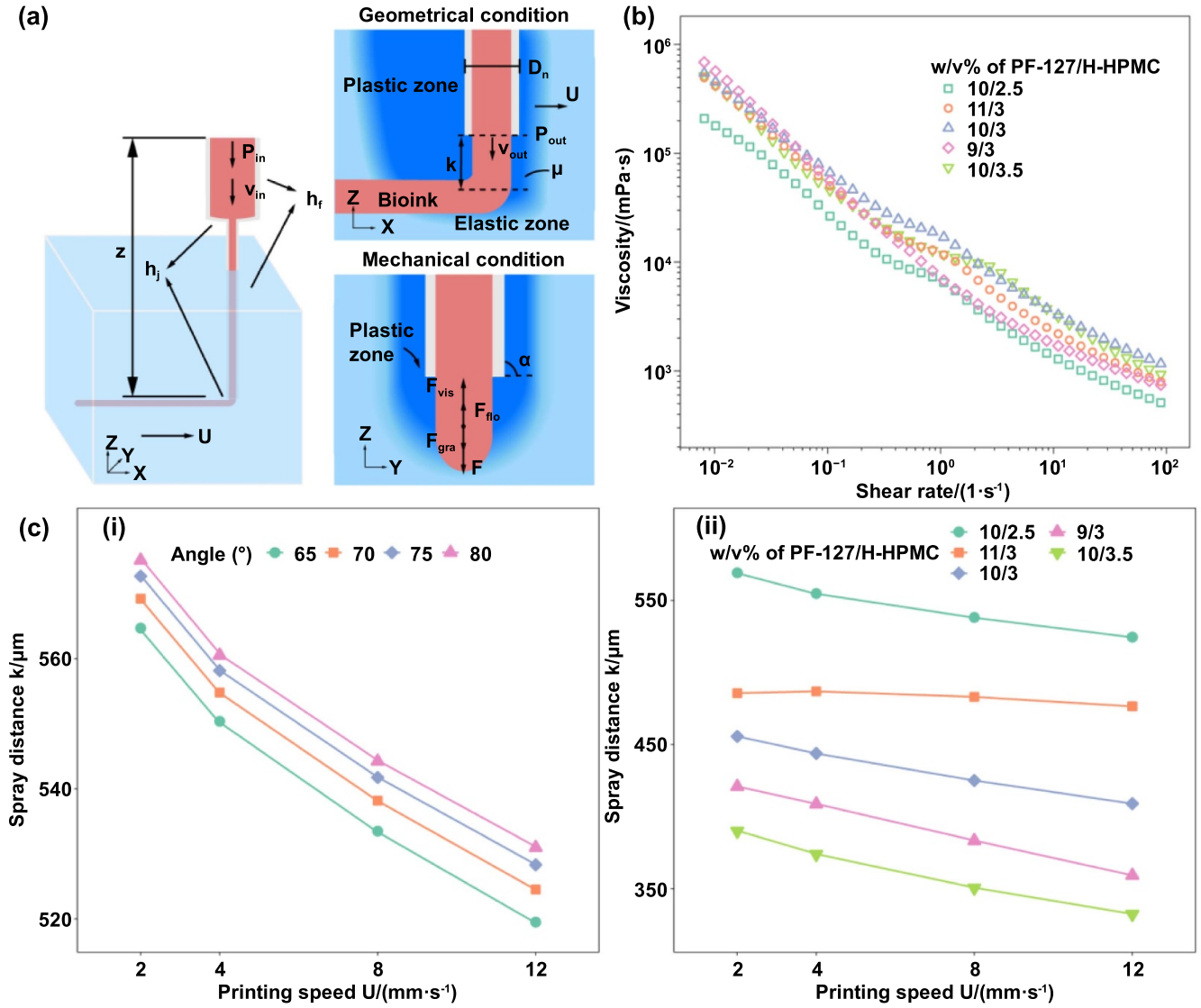


Figure 2. Evaluation of bioink extrusion distance. (a) A schematic diagram of embedded printing. (b) Shear thinning characteristics of the embedding medium. (c) The extruded distance in theory with different (i) nozzle angles and (ii) embedding mediums.

The extruded distance k could be calculated by integrating the velocity with respect to time:

$$k = \int_{t_1}^t v dt. \quad (6)$$

By substitute equation (5) in to equation (6), k could be written as:

$$k = \frac{Fl + (mg - \rho_{bath}gV)l \sin \alpha}{\mu A} (t - t_1) + \left(\frac{m l^2 [F + (mg - \rho_{bath}gV) \sin \alpha] - v_1 m l \mu A}{\mu^2 A^2} \right) \times \left(e^{-\frac{\mu A (t - t_1)}{m l}} - 1 \right) \quad (7)$$

where v_1 is the velocity of bioink at the time t_1 . The change of viscosity with velocity field of embedding medium could be approximated [29]:

$$u = U e^{-\frac{k}{f D_n}} \quad (8)$$

$$\mu = f(u) \quad (9)$$

where u is the local velocity of the embedding medium, U is the nozzle translation velocity (printing speed), k is the distance from the nozzle, D_n is the nozzle diameter, and f is a parameter related to the embedding medium. Viscosity is considered as a function of local velocity which can be obtained through rheological test (figure 2(b)).

In equation (7), the force transferred by bioink during extrusion F , was determined by the outlet pressure P_{out} of the bioink at the exit of nozzle, which was dependent on the extrusion pressure P_{in} . According to the Bernoulli equation for viscous fluids, with a given P_{in} , syringe and nozzle geometry, P_{out} could be calculated via the dynamics in the syringe and nozzle:

$$P_{\text{out}} = P_{\text{in}} + \frac{1}{2}\rho(v_{\text{in}}^2 - v_{\text{out}}^2) + \rho g(z - h_w) \quad (10)$$

$$F = A_r P_{\text{out}} \quad (11)$$

where P_{in} is the initial pressure of the bioink in the syringe, ρ is the density of the bioink, v_{in} and v_{out} are the velocity of the bioink, z is the height of the bioink, P_{out} is the pressure of the bioink extruded from the nozzle, A_r is the applied area of pressure, h_w is the loss of non-mechanical energy which is the summation of friction loss h_f and local loss h_j :

$$h_w = \sum h_f + \sum h_j \quad (12)$$

$$h_f = \lambda \frac{l_f v^2}{2dg} \quad (13)$$

$$h_j = \xi \frac{v^2}{2g} \quad (14)$$

$$\lambda = \frac{64}{\text{Re}} \quad (15)$$

where λ is a coefficient related to the friction loss which can be empirically calculated as equation (15), l_f is the characteristic axial dimension of the bioink flow, v is the average velocity of the bioink, d is the characteristic radii dimension of the bioink flow, ξ is a coefficient related to the local loss which is estimated to be 0.5 according to empirical results, Re is the Reynolds number. The friction loss flow through the syringe or nozzle was taken into account, while the local loss happened when the bioink was extruded into the nozzle or embedding medium. Therefore, we could calculate the pressure P_{out} , and therefore force F on the bioink during extrusion.

During an infinitesimal period of time ($t_1 - t_0$), we assume that the forces applied on the bioink remain constant. Given the initial conditions (printing speed, nozzle angle, and rheological characteristics of embedding medium) and constant parameters (nozzle diameter, density of the embedding medium, disturbance range, friction loss coefficient) (table S1), the bioink speed v and extruded distance k_1 within a time step can be calculated through equations (5) and (7). As the viscosity of the embedding medium, speed and extruded distance in the previous timestep are functions of bioink speed v and extruded distance k , the initial conditions of next timestep ($t_2 - t_1$) can be determined iteratively until speed v converges to 0. The total extruded distance k is the summation of the extruded distance k_1 through k_n in each time segment (figure 2(c)). This extruded distance k is defined as the displacement from the extruded bioink exit nozzle to fully stop in embedding medium. With a tilted nozzle, the displacement component in vertical and horizontal direction can be precisely controlled, enhancing the deposition precision of the bioink.

3.2. Simultaneous embedded printing with multi-material

To address the current challenges existing in embedded printing, a simultaneous printing method was proposed to realize the construction of multi-layered structure in the embedding medium with multiple materials (figure 3). Briefly, in one horizontal layer, adjacent strands of different bioinks were deposited simultaneously by individually controlled nozzles, to minimize the disturbance, enhance the lateral attachments and produce a clear interface between the inner and outer layer structures. The nozzle tips should be kept close, but not directly attached during printing to deposit bioinks within a single liquefied region of the embedding medium (figure 3(a)). In the liquefied region, the embedding medium had low viscosity due to shear, resulting in small disturbance to the extruded bioinks within this region. As the bioinks exited the nozzle, they could travel in the liquefied region for a short distance before they reached each other and remain *in situ*. During the printing process, multiple nozzles were simultaneously moved according to multiple adjacent motion tracks accompanied by extrusion and deposition of various bioinks at the same time.

As shown in figure 1, the viscosity of the embedding medium, the angle of the nozzle and the printing speed would affect the bioink extruded distance k , therefore affecting the attachment of the filaments in the simultaneous printing process. During the experiments, a consistent flow rate of bioink was used. The influence of different nozzle angles and printing speeds on the adhesion of adjacent filaments were investigated (figure 3(c)). According to the previously mentioned printing parameters, the extrusion pressure had an obvious effect on the movement of bioink during the extrusion process. In contrast, the influence of viscosity gradient of the embedding medium, and the effect of gravity and buoyancy were weak. Therefore, when changing the printing speed and nozzle angle, the extruded distance remained in a certain range with little variation. However, with different nozzle angles relative to the horizontal plane, the projection of the extruded distance k was different. Thus, the relative distance between the nozzle tips could be larger while still keeping the attachment of the adjacent filaments, which helped avoid the interference between nozzles. This distance was determined by filament diameter, extruded distance and relative distance between nozzles. With nozzles of the same diameter, the required minimum extruded distance k'_1 and k'_2 could be calculated:

$$\begin{aligned} & k'_1 \cos \frac{\alpha_1 + \alpha_2}{2} + k'_2 \cos \frac{\alpha_1 + \alpha_2}{2} \\ & + \sqrt{\left(\frac{D_1 + D_2}{2}\right)^2 - (k'_2 - k'_1)^2 \sin^2 \left(\frac{\alpha_1 + \alpha_2}{2}\right)} \\ & = \sqrt{D_n^2 \left(\sin \frac{\alpha_1 + \alpha_2}{2}\right)^2 + D_a^2 + D_n D_a (\sin \alpha_1 + \sin \alpha_2)} \end{aligned} \quad (16)$$

where D_1 and D_2 are the diameter of extruded bioink, α_1 and α_2 are each angle of the adjacent nozzles, D_n is the diameter of

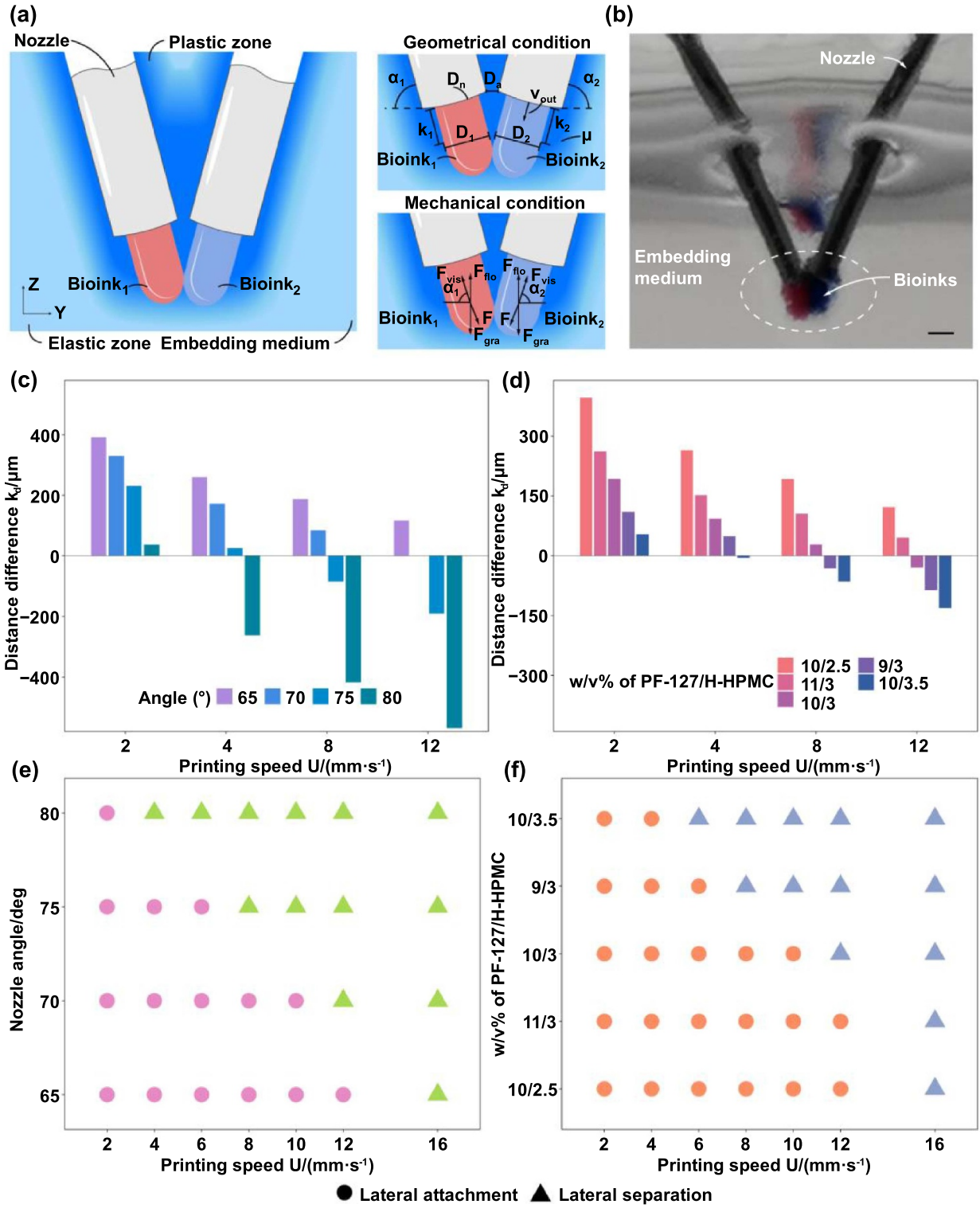


Figure 3. Phase diagram of filament attachment. (a) A schematic diagram of simultaneous printing. (b) Example of bioink deposition process (scale bar: 500 μm). (c), (d) The subtraction of the extruded distance and the required extruded distance in theory. Printing phase diagram of printing speed and nozzle angle (e) printing speed and embedding medium (f) on filament attachment.

the nozzle, D_a is relative distance between the tip of nozzles. When the required minimum extruded distance k'_1 was equal to k'_2 which could be considered as k' , A difference k_d could be defined as equation (17)

$$k_d = k - k'. \quad (17)$$

If k_d was greater than zero, the filaments could attach laterally in theory, and when k_d was less than zero, the filaments

would separate. With two nozzles at the same tilted angle, the minimum extruded distance needed to reach the attachment state is calculated. When printing speed increased, the diameter of the printed filament decreased, which required a larger extruded distance. Moreover, the distance required for attachment is also affected by the nozzle angle. A smaller nozzle angle results in a decreased required extruded distance, making it easier for the two bioinks to achieve lateral attachment. In the experimental results, we found that lateral attachment was more difficult to achieve at high printing speed while maintaining the same nozzle angle, which was consistent with our theoretical analysis (figure 3(e)). The experimental results showed that lateral attachment occurred with decreased nozzle angles under the same printing speed, which was also as expected. But having the nozzle angle too small would cause collision between the nozzle and the embedding medium container, increasing the printing difficulty especially for large scaled structures. Therefore, the angle of the nozzle should be selected in an appropriate range to match printing speed, structure size and other printing parameters.

We also investigated the effect of embedding medium characteristics on bioink attachment. The embedding media used in this research have regulatable rheological properties [30]. We also calculated the difference between the extruded distance and the minimum extruded distance required to reach the attachment based on the fitting curves mentioned above (figure 3(d)). At the same printing speed, embedding medium with low yield stress would result in a large velocity field with lower viscosity. Therefore, the extruded bioink was subjected to a small viscous effect and therefore stopped further away from the nozzle. This phenomenon was demonstrated by our calculation results. In experiments, we observed that in the embedding medium with low yield stress, adjacent filaments could be in contact with each other at high nozzle movement speed, whilst that could not occur in the embedding medium with low yield stress (figure 3(f)). The experiment results were consistent with our theoretical analysis. If the yield stress of the embedding medium was too low, the supporting ability to the printed structure would also reduce and degrade the morphological feature preservation of the structure. Therefore, the concentration of embedding medium should be selected within a reasonable range.

3.3. Quantitative characterization of simultaneous bioprinting

In the process of printing, the morphology of the printed filament plays a significant role in the formation of the final structure. As the fundamental unit of 3D printed structure, the morphology characteristics of the filament can be used as the characterization index of the printing process. Two features of the printed filaments are evaluated: aspect ratio and filament width (figure 4(a)), the aspect ratio f is defined as:

$$f = \frac{D}{H} \quad (18)$$

where D is the width of the filament in horizontal direction and H is the height of the filament in vertical direction.

We conducted an evaluation of the morphology of individual printed filament. The value of aspect ratio f close to 1 is preferred, as it indicates that the filament cross-section is closer to the circle, which is consistent with the setting in the slicing software, so that the complex structures designed can be printed accurately. In the previous study, aspect ratio of printed filaments could be expressed by linear regression as follows [30]:

$$f = a \times \mu_t + b \quad (19)$$

where a and b are fitted coefficients. μ_t is the transient viscosity of embedding medium obtained from the shear rate sweep. Ideally, the cross-section shape of the filament was considered to be consistent. We could assume that the flow, cross-section area and printing speed satisfied the following formula:

$$Q = A \times U \quad (20)$$

where Q is the volume flow rate, A is the cross-section area of the printed filament, and U is the printing speed. Theoretically, the area of a filament was directly proportional to the product of its height and width. Therefore, the width of the filaments, transient viscosity and printing speed could be substitute into equation (18) with a constant extrusion flow rate:

$$D = \sqrt{\frac{c \times \mu_t + d}{U}} + e \quad (21)$$

where c , d and e are fitted coefficients. We obtained equation (21) by rheological experiment and printing experiment, and the results showed a high goodness of fit ($R^2 = 0.93$) (figure 4(b)). According to equation (21), for a constant flow rate, with the increase of the printing speed or the viscosity of the embedding medium, the width of the printed filament decreased significantly, thus we could predict the morphology of individually printed filaments. We defined the similarity index S_d which was the ratio of the morphological features of the filaments by printing simultaneously and individually to evaluate the approximation level of filament morphology by the two printing methods,

$$S_d = \frac{D_{\text{simultaneous}}}{D_{\text{individual}}} \quad (22)$$

The aspect ratio of the simultaneous printing filaments was defined as the average of the respective aspect ratio. And the width of the simultaneous printing filaments was defined as the average of the respective filament width. The morphology of laterally attached filaments formed by simultaneous printing and single filament by individual printing were evaluated (figure 4(d)).

The width of the individually printed filament could be predicted according to equation (21), as a function of the embedding medium viscosity and the printing speed, these width dimensions were used as a baseline to evaluate the printed filament resolutions. For simultaneous printing, it was difficult to directly estimate the filament width with printing parameters due to the complexity of the printing process. We therefore proposed the similarity index S_d to predict the nozzle induced

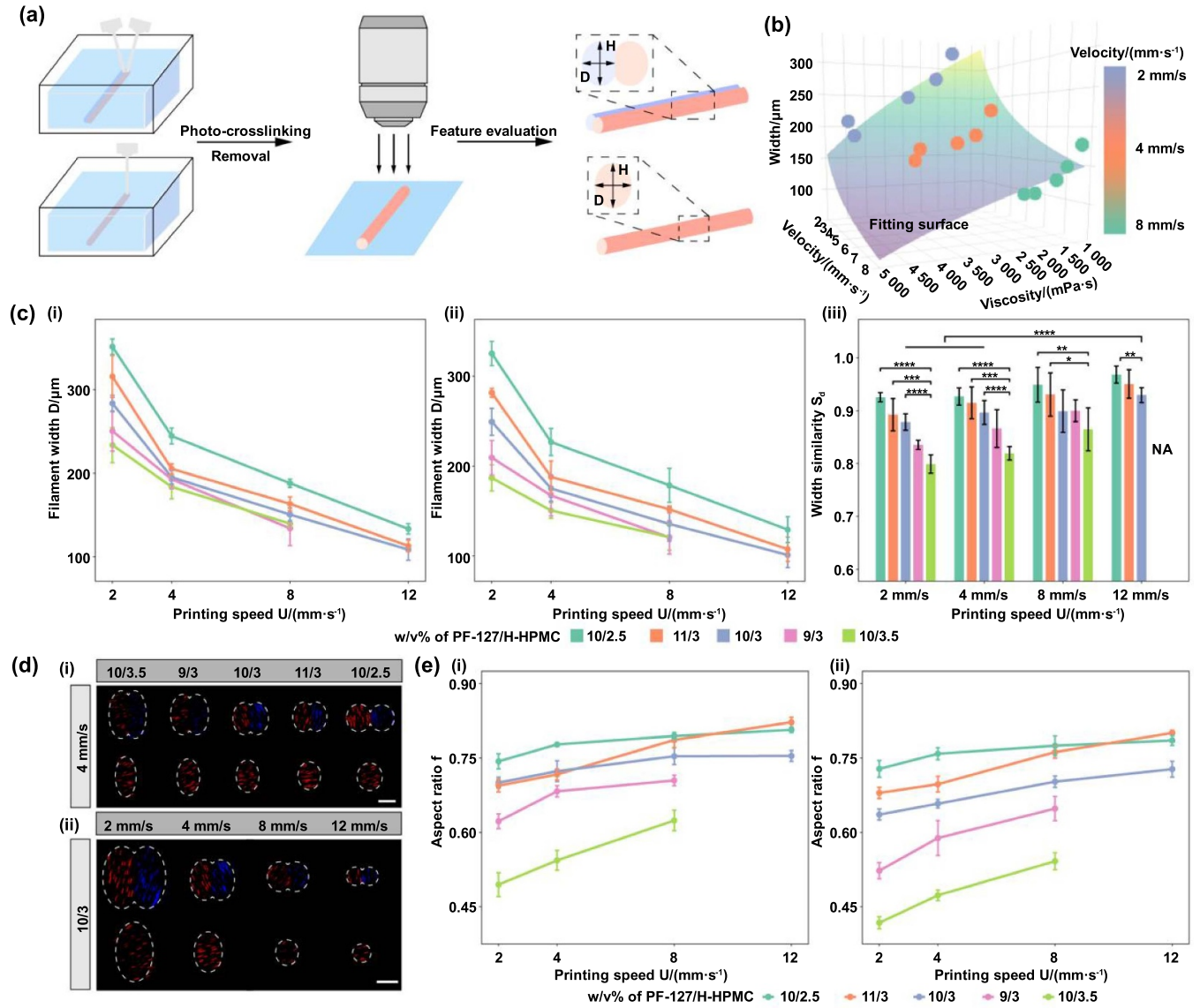


Figure 4. Quantitative characterization of simultaneous bioprinting. (a) A schematic of the investigation of the characterization. (b) The fitting results of printing speed and embedding medium viscosity on the width of the filament. (c) The width of filament which were printed (i) individually and (ii) simultaneously in different embedding medium at various printing speeds. (iii) Compare with the width of filaments printed individually and simultaneously. (d) (i) Cross-sections of filaments that were printed in various baths at $4\text{ mm}\cdot\text{s}^{-1}$. (ii) Cross-sections of filaments that were printed in 10% PF-127/3% H-HPMC at various printing speeds (scale bar: $200\text{ }\mu\text{m}$). (e) The aspect ratio of filaments which were printed (i) individually and (ii) simultaneously in different embedding medium at various printing speeds.

effects of the additional nozzle used in the simultaneous printing method. As the results shown in figure 4(c), the minimum width of the printed filaments for both printing methods was around $100\text{ }\mu\text{m}$. The similarity index S_d was always less than 1, but for a greater printing speed the similarity index S_d was greater and closer to 1. This indicated that when the shear rate of the medium was at a high level, and the local viscosity of embedding medium was low, the additional printing nozzles used in the simultaneous printing would have less impact on the printing resolution. Thus, the proposed simultaneous printing method might work better at a higher printing speed.

In order to construct an accurate three-dimensional structure, precise control over the height of the printed filaments is crucially important. The width and the height of the filaments

were highly related, thus we defined the aspect ratio of a filament cross-section as equation (18), to evaluate the effect of additional printing nozzle on the vertical direction. As the results shown in figure 4(e), the aspect ratio f was always less than 1, indicating the height was always greater than the width of an embedded printed filament. This might be induced by the up flow of the ink when the nozzle moved away and the crevasse started to heal. As expected, the filament printed in the medium with longer thixotropic time scale had a lower aspect ratio. For the proposed printing method, due to the existence of an additional nozzle, the nozzle induced crevasse was almost double sized compared with the conventional printing method, embedding medium with lower local viscosity was preferred, so the height of the printed filament could be controlled.

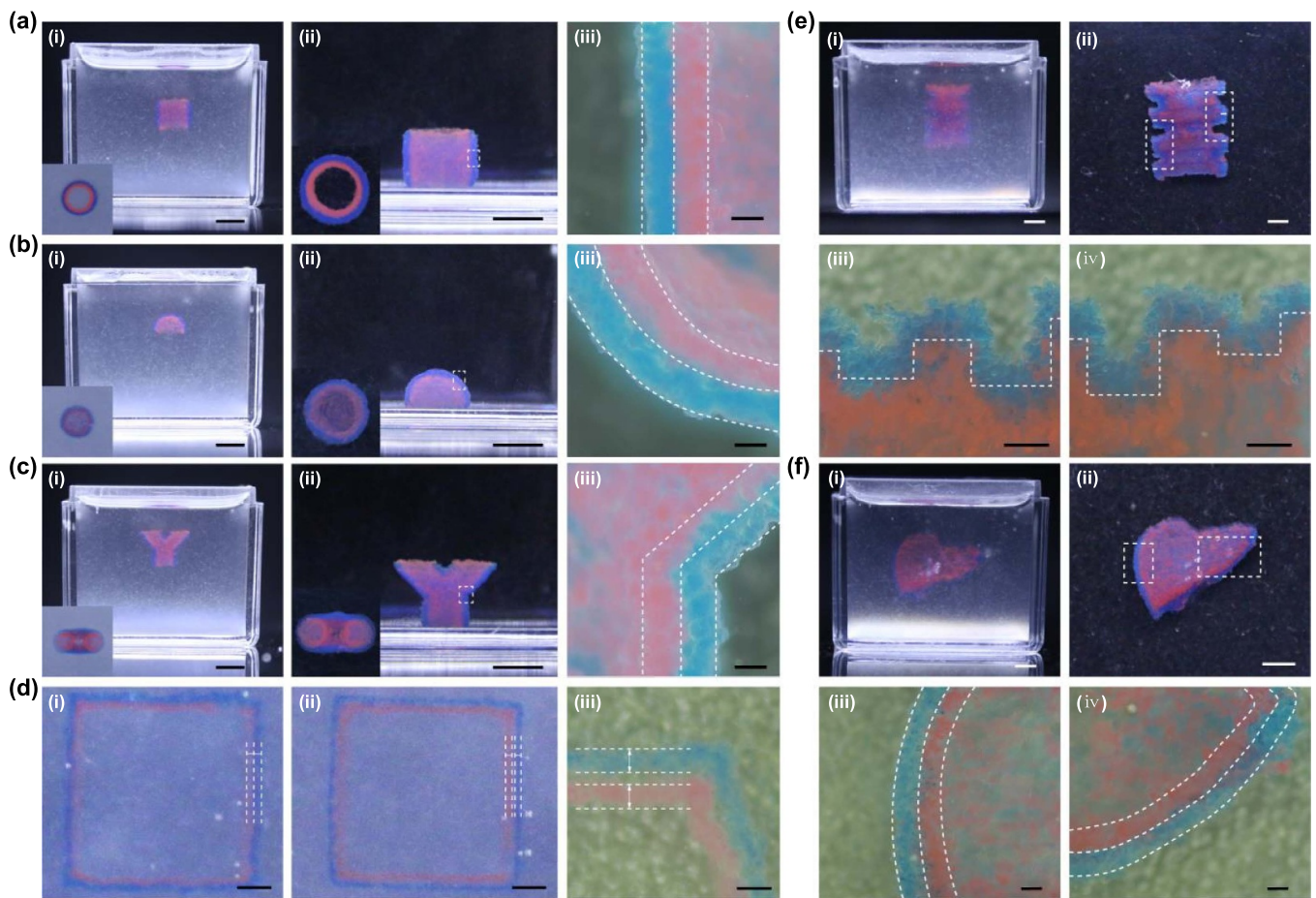


Figure 5. Multilayer constructions printed simultaneously. The front view of (a) double-layer hollow straight tubes (b) double-layer hemisphere and (c) double-layer Y-shaped tube in (i) the embedding medium and (ii) PBS (scale bar: 3 mm). The lower left corner is the corresponding top view. (iii) Axial cross section of (a) double-layer hollow straight tubes (b) double-layer hemisphere and (c) double-layer Y-shaped tube (scale bar: 200 μm). The parts between the dotted lines are structures made of different materials. (d) The multilayer rectangular structures were printed simultaneously (i) and sequentially (ii) under the same trajectory (scale bar: 2 mm). (iii) Local magnification of sequentially printed structures (scale bar: 1 mm). (e) The double-layer structure of intestine in (i) the embedding medium and (ii) PBS (scale bar: 3 mm). (iii–iv) Local amplification of printing structure (scale bar: 500 μm). (f) The similar double-layer structure of liver. (iii–iv) Local amplification of printing structure (scale bar: 500 μm).

Based on the experimental results above, with the selected printing parameters and embedding medium, high-precision filaments could be simultaneously printed with good position fidelity, which enabled us to manufacture complex heterogeneous structures.

3.4. Freeform writing of heterogeneous structures

There are many multicellular tissues, such as blood vessels and the heart, which are composed of complex tubular and capsule structures. Therefore, we selected common multi-layer tubular and capsule structures as printing demonstrations. Three-dimensional models were sliced and toolpaths were generated, and different materials were marked with colour dyes for different layers. We chose different three-dimensional structures, so that in the axial direction the boundary lines between the two layers of different bioinks were straight line, curves and broken line. Specifically, double-layer hollow straight tube, double-layer hemisphere, and double-layer Y-shaped

tube were printed in the embedding medium, respectively (figures 5(a)–(c)). The container was exposed in UV light for 5 min, so the printed structures were crosslinked and then released from the medium. The printed samples were transferred into 37 °C PBS and showed good structure integrity. In the process of removing the printing structure from the embedding medium and cleaning in PBS, there was no delamination observed between layers. In particular, from the top view, it could be clearly seen that two layers with different colours bonded together to form a uniform multi-layer structure. In order to further evaluate the attachment between the multi-layer structures and the printing accuracy, we further examined the printed three-dimensional structures by cutting them along the axial direction and observing the cross-sections with a bright field microscope. As shown in the profiles, we could observe that the two layers of the structure were closely attached together while still maintaining a clear interface between two layers, indicating that uncontrolled mixture is minimal. Furthermore, there was no embedding medium

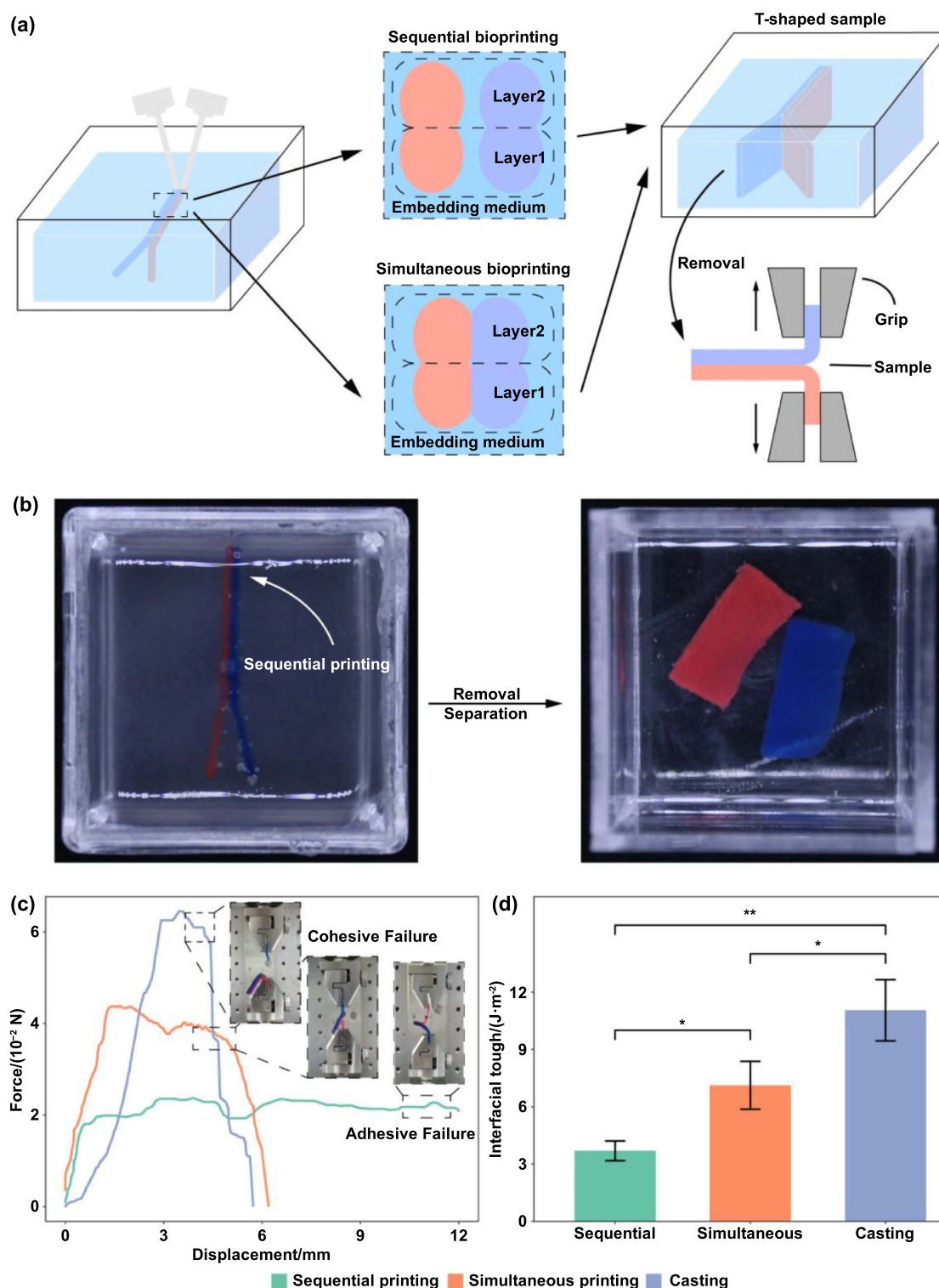


Figure 6. Results of peeling test. (a) A schematic of sample preparation and peeling test. (b) Sequentially printed samples can be separated into two parts after being removed from the embedding medium. (c) Representative test data of samples obtained by three preparation methods. (d) Summary of measured interfacial toughness for samples obtained by three preparation methods.

remained between the two layers. The thickness of the two layers was identical and measured as approximately $200 \mu m$, proving that our printing parameter selection could precisely control the accuracy of the printing structure and maintained good consistency with the designed parameters. These 3D

structures were further printed with bioinks of different rheological properties and crosslinking methods (5%w/v GelMA and 3%w/v Alginate) with same printing parameters (figure S5). The axial cut profile also showed a good position fidelity of the two sub filaments. During printing, the sodium alginate

bioink quickly formed a crosslinked surface as the filament deposited into the embedding medium, which made the trans-layer fusion behaviour between different inks different.

We also printed two of concentric rectangles with simultaneous printing or sequential printing method with same printing trajectory and printing conditions, to evaluate the bonding of the multilayer structures. While the sequential printing result showed the existence of embedding medium between the two printed layers, this was not observed with simultaneous printing (figure 5(d)(i)–(ii)). With the microscope, we could observe the separation of the two layers more clearly (figure 5(d)(iii)). The results indicated that simultaneous printing could achieve better bonding of multilayer structures under certain printing conditions. Finally, we printed a double-layer structure of small intestine and liver that had a similar structure to the circular fold shape of the native organ (figures 5(e)–(f)). Magnifying the sections of the two organ models showed that the two-layer structure achieved good adhesion. For structures with complex shapes, simultaneous printing method could accurately print the double-layer structure with optimal attachment and morphology.

3.5. Evaluation of the structural integrity of the printed structure

The structural integrity problems of the multi-layered structure printed by the embedding printing method has been reported [23, 24]. Therefore, a peeling test was carried out to investigate the bonding strength between simultaneously printed specimen, results were compared with the casted and sequentially printed specimen. The peeling test results of three groups of specimens have shown failure types (figure 6). In the casted and simultaneous printed specimens, tensile failures occurred on one of the tabs before the grips reached the maximum test range, which showed that the bonding strength of these two cases were greater than the material strength, and the casted GelMA had a better ultimate break strength. While for the sequentially printed specimens, they were gradually peeled and no tensile failure were observed before the maximum range, which means for the sequentially printed specimens, the bonding strength was less than the strength of the soft material itself.

The normalized maximum force relative to the sample width was chosen as the evaluation characteristic of interfacial toughness. Our results showed that the bonding strength of the samples by simultaneous printing was significantly greater than that of the samples by sequential printing under the same trajectory. It could be induced by the contaminated embedding medium between the two tabs during the sequential printing, which created discrete interfaces. The embedding medium used in this research was designed to be removed after printing and it could not be crosslinked, as a result it was not offering any tensile strength. Therefore, the bonding strength would decrease if any contaminated medium was kept between inner and outer layers of the printed structure. The proposed simultaneous printing method had minimized the chance of the contamination of the embedding medium for the 3D printing of multi-layered and multi-material structures, providing a direct

solution of the present structural integrity problems for such structures.

4. Conclusion

In this study, a simultaneous multi-material embedded printing method is proposed, which enables us to print multi-layered heterogeneity structures with better structural integrity and precision. The dynamics of the extruded bioink is analysed with a simplified model and verified in experiments. It is found that with the commonly used printing parameters and embedding medium, the extruded bioink can travel up to about 500 μm from the nozzle tip before it is fully stopped and kept in the bath. This feature partially explains why printed structures during embedded printing often delaminate in the horizontal direction when nozzles are typically oriented in the vertical direction. Utilizing the dynamic characteristics of the bioink, we have proposed a multi-material printing method that employs multiple individually controlled nozzles oriented at tilted angles, to deposit different materials into a single crevasse in the embedding medium, the filaments are firmly fused and deposited in an accurate spatial position. By adjusting the printing speed and the rheology of the embedding medium, the simultaneous printing method can better control the morphology of the structure and improve printing accuracy. In order to verify the proposed simultaneous printing method, a range of tubular and globular multilayer structures were printed. The results showed good precision with each layer less than 200 μm in thickness. The bonding strength between layers was also found to have doubled to 7.12 J m^{-2} , compared to the conventional sequential printing method. The primary challenge on the proposed printing method is designing the toolpath trajectory for the simultaneous printing. This trajectory must ensure the proper orientation of multiple sub-filaments while avoiding the physical interference between nozzles within a millimetre space. When using bioinks with different cross-linking mechanisms, the inter-layer fusion behaviours become complex. Therefore, further investigation of fusion control strategies is required to achieve optimal results in the future. Nevertheless, the proposed printing method offers the potential to fabricate multi-material multilayer structures with high precision and good structural integrity, making it a promising technique in the manufacturing of heterogeneous structures with soft biomaterials and soft composites. We also believe that the simultaneous printing method has a potential to be used in multi-material additive manufacturing applications of other polymer materials [31, 32], which also required a good precision as well as the structural fidelity.

Acknowledgments

We would like to thank the support by National Key Research and Development Program of China (2018YFA0703000), National Natural Science Foundation of China (Grant No. 52105310), Natural Science Foundation of Zhejiang Province (Grant No. LDQ23E050001) and the Starry Night Science

Fund of Zhejiang University Shanghai Institute for Advanced Study (Grant No. SN-ZJU-SIAS-004).

Author contributions

Z G, J Y, H Y, R Z, H Z, and conceived the concept of this work. Z G, J Y, and H Z established the theoretic models. Z G, Q L, P L, conducted the experiments and analysis. Z G and H Z wrote the manuscript. J Y, and R Z, proofread and edited the final manuscript.

Conflict of interest

The authors declare no competing financial interest.

ORCID iD

Hongzhao Zhou  <https://orcid.org/0000-0001-7377-0741>

References

- [1] Ashammakhi N, Hasan A, Kaarela O, Byambaa B, Sheikhi A, Gaharwar A K and Khademhosseini A 2019 Advancing frontiers in bone bioprinting *Adv. Healthcare Mater.* **8** 1801048
- [2] Ashammakhi N, Ahadian S, Fan Z J, Suthiwanich K, Lorestani F, Orive G, Ostrovidov S and Khademhosseini A 2018 Advances and future perspectives in 4D bioprinting *Biotechnol. J.* **13** 1800148
- [3] Zhu Y Z, Joralmón D, Shan W T, Chen Y Y, Rong J H, Zhao H Y, Xiao S Q and Li X J 2021 3D printing biomimetic materials and structures for biomedical applications *Bio-Des. Manuf.* **4** 405–28
- [4] Tavafoghi M et al 2021 Multimaterial bioprinting and combination of processing techniques towards the fabrication of biomimetic tissues and organs *Biofabrication* **13** 042002
- [5] Wang P J, Sun Y Z, Shi X Q, Shen H X, Ning H H and Liu H T 2021 3D printing of tissue engineering scaffolds: a focus on vascular regeneration *Bio-Des. Manuf.* **4** 344–78
- [6] Rawal P, Tripathi D M, Ramakrishna S and Kaur S 2021 Prospects for 3D bioprinting of organoids *Bio-Des. Manuf.* **4** 627–40
- [7] Dalton P D, Woodfield T B F, Mironov V and Groll J 2020 Advances in hybrid fabrication toward hierarchical tissue constructs *Adv. Sci.* **7** 1902953
- [8] Zhou H Z, Liu P, Gao Z Q, Li Q, Lv W K, Yin J, Zhang B, Yang H Y and Ma L 2022 Simultaneous multimaterial multimethod bioprinting *Bio-Des. Manuf.* **5** 433–6
- [9] Merceron T K, Burt M, Seol Y J, Kang H W, Lee S J, Yoo J J and Atala A 2015 A 3D bioprinted complex structure for engineering the muscle-tendon unit *Biofabrication* **7** 035003
- [10] Shim J H, Lee J S, Kim J Y and Cho D W 2012 Bioprinting of a mechanically enhanced three-dimensional dual cell-laden construct for osteochondral tissue engineering using a multi-head tissue/organ building system *J. Micromech. Microeng.* **22** 085014
- [11] Larson N M, Mueller J, Chortos A, Davidson Z S, Clarke D R and Lewis J A 2023 Rotational multimaterial printing of filaments with subvoxel control *Nature* **613** 682–8
- [12] Kang D G, Hong G, An S, Jang I, Yun W S, Shim J H and Jin S 2020 Bioprinting of multiscaled hepatic lobules within a highly vascularized construct *Small* **16** 1905505
- [13] Goh G L, Zhang H N, Chong T H and Yeong W Y 2021 3D printing of multilayered and multimaterial electronics: a review *Adv. Electron. Mater.* **7** 2100445
- [14] Ge Q, Sakhaei A H, Lee H, Dunn C K, Fang N X and Dunn M L 2016 Multimaterial 4D printing with tailorable shape memory polymers *Sci. Rep.* **6** 31110
- [15] Skylar-Scott M A, Mueller J, Visser C W and Lewis J A 2019 Voxlated soft matter via multimaterial multinozzle 3D printing *Nature* **575** 330–5
- [16] Ning L Q, Mehta R, Cao C, Theus A, Tomov M, Zhu N, Weeks E R, Bauser-Heaton H and Serpooshan V 2020 Embedded 3D bioprinting of gelatin methacryloyl-based constructs with highly tunable structural fidelity *ACS Appl. Mater. Interfaces* **12** 44563–77
- [17] Afghah F, Altunbek M, Dikyol C and Koc B 2020 Preparation and characterization of nanoclay-hydrogel composite support-bath for bioprinting of complex structures *Sci. Rep.* **10** 5257
- [18] Lee A, Hudson A R, Shiwardski D J, Tashman J W, Hinton T J, Yerneni S, Bliley J M, Campbell P G and Feinberg A W 2019 3D bioprinting of collagen to rebuild components of the human heart *Science* **365** 482–7
- [19] Bhattacharjee T, Zehnder S M, Rowe K G, Jain S, Nixon R M, Sawyer W G and Angelini T E 2015 Writing in the granular gel medium *Sci. Adv.* **1** e1500655
- [20] Li Q, Jiang Z R, Ma L, Yin J, Gao Z Q, Shen L Q, Yang H Y, Cui Z F, Ye H and Zhou H Z 2022 A versatile embedding medium for freeform bioprinting with multi-crosslinking methods *Biofabrication* **14** 035022
- [21] Noor N, Shapira A, Edri R, Gal I, Wertheim L and Dvir T 2019 3D printing of personalized thick and perfusable cardiac patches and hearts *Adv. Sci.* **6** 1900344
- [22] Uchida T and Onoe H 2019 4D printing of multi-hydrogels using direct ink writing in a supporting viscous liquid *Micromachines* **10** 433
- [23] Karyappa R and Hashimoto M 2021 Freeform polymer precipitation in microparticulate gels *ACS Appl. Polym. Mater.* **3** 908–19
- [24] Hinton T J, Hudson A, Pusch K, Lee A and Feinberg A W 2016 3D printing PDMS elastomer in a hydrophilic support bath via freeform reversible embedding *ACS Biomater. Sci. Eng.* **2** 1781–6
- [25] Hua W J, Mitchell K, Kariyawasam L S, Do C, Chen J H, Raymond L, Valentin N, Coulter R, Yang Y and Jin Y F 2022 Three-dimensional printing in stimuli-responsive yield-stress fluid with an interactive dual microstructure *ACS Appl. Mater. Interfaces* **14** 39420–31
- [26] Jin Y F, Chai W X and Huang Y 2017 Printability study of hydrogel solution extrusion in nanoclay yield-stress bath during printing-then-gelation biofabrication *Mater. Sci. Eng. C* **80** 313–25
- [27] Tokpavi D L, Magnin A and Jay P 2008 Very slow flow of Bingham viscoplastic fluid around a circular cylinder *J. Non-Newton. Fluid Mech.* **154** 65–76
- [28] Walker S, Lingle E, Troxler N, Wallin T, Healy K, Mengüç Y and Davidson J R 2021 Predicting interfacial layer adhesion strength in 3D printable silicone *Addit. Manuf.* **47** 102320
- [29] Grosskopf A K, Truby R L, Kim H, Perazzo A, Lewis J A and Stone H A 2018 Viscoplastic matrix materials for embedded 3D printing *ACS Appl. Mater. Interfaces* **10** 23353–61
- [30] Li Q, Ma L, Gao Z Q, Yin J, Liu P, Yang H Y, Shen L Q and Zhou H Z 2022 Regulable supporting baths for embedded printing of soft biomaterials with variable stiffness *ACS Appl. Mater. Interfaces* **14** 41695–711
- [31] Bandyopadhyay A and Heer B 2018 Additive manufacturing of multi-material structures *Mater. Sci. Eng. R* **129** 1–16
- [32] Loke G, Yuan R, Rein M, Khudiyev T, Jain Y, Joannopoulos J and Fink Y 2019 Structured multimaterial filaments for 3D printing of optoelectronics *Nat. Commun.* **10** 4010